Acta Crystallographica Section D
Biological Crystallography
ISSN 0907-4449

UV laser-excited fluorescence as a tool for the visualization of protein crystals mounted in loops

Xavier Vernede,[a] Bernard Lavault,[b] Jeremy Ohana,[a] Didier Nurizzo,[c] Jacques Joly,[a] Lilian Jacquamet,[a] Franck Felisaz,[b] Florent Cipriani[b] and Dominique Bourgeois[a,c]*

[a]LCCP, UMR 5075, IBS–CEA/CNRS/UJF, 41 Rue Jules Horowitz, 38027 Grenoble CEDEX 1, France, [b]EMBL, 10 Rue Jules Horowitz, BP 181, 38042 Grenoble CEDEX 9, France, and [c]ESRF, 6 Rue Jules Horowitz, BP 220, 38043 Grenoble CEDEX, France

Correspondence e-mail: dominique.bourgeois@ibs.fr

Received 12 October 2005
Accepted 12 December 2005

PDB References: insu_1sec, 2c8q; insu_60sec, 2c8r; lyso_1sec, 2c8o, r2c80sf; lyso_60sec, 2c8p.

Structural proteomics has promoted the rapid development of automated protein structure determination using X-ray crystallography. Robotics are now routinely used along the pipeline from genes to protein structures. However, a bottleneck still remains. At synchrotron beamlines, the success rate of automated sample alignment along the X-ray beam is limited by difficulties in visualization of protein crystals, especially when they are small and embedded in mother liquor. Despite considerable improvement in optical microscopes, the use of visible light transmitted or reflected by the sample may result in poor or misleading contrast. Here, the endogenous fluorescence from aromatic amino acids has been used to identify even tiny or weakly fluorescent crystals with a high success rate. The use of a compact laser at 266 nm in combination with non-fluorescent sample holders provides an efficient solution to collect high-contrast fluorescence images in a few milliseconds and using standard camera optics. The best image quality was obtained with direct illumination through a viewing system coaxial with the UV beam. Crystallographic data suggest that the employed UV exposures do not generate detectable structural damage.

1. Introduction

In recent years, ambitious structural proteomics projects have been launched that aim at elucidating the three-dimensional structures of the vast number of proteins encoded by entire genomes (see, for example, Stevens *et al.*, 2001). X-ray crystallography and synchrotron radiation are central to these projects. Considerable efforts in the automation of all steps leading from gene to protein structure have been undertaken (Abola *et al.*, 2000; Lesley *et al.*, 2002; Terwilliger *et al.*, 2003; see also the *Proceedings of the CCP4 Study Weekend* 2002 published as the November 2002 issue of *Acta Crystallographica Section D*). Robots for cloning (Yokoyama, 2003), purification (Kim *et al.*, 2004), crystallization (McPherson, 2004; Stevens, 2000) and crystal mounting on synchrotron beamlines (Cohen *et al.*, 2002; Karain *et al.*, 2002; Ohana *et al.*, 2004; Pohl *et al.*, 2004; Snell *et al.*, 2004) have been constructed. In a growing number of cases, diffraction data may also be recorded and a protein model built automatically (Holton & Alber, 2004; Liu *et al.*, 2005; Ness *et al.*, 2004; Panjikar *et al.*, 2005). However, the reliable identification of a crystal within its sample holder for alignment along the X-ray beam remains problematic. Protein crystals, often as small as 10 μm or less in size, are bathed in a cryoprotectant solution and held by surface tension in various types of loops usually larger than the crystal itself. Localization of the crystal within the loop, even for the expert, may therefore prove extremely difficult under illumination by visible light. Indeed, even with excellent

microscopes, absorption, diffusion and/or refraction effects may combine to completely obscure the sample.

A number of methods have been proposed to overcome the difficulties of automated crystal detection and centring. In the first step, it is relatively easy to detect and centre the loop holding the crystal (Karain *et al.*, 2002; Snell *et al.*, 2004). This solution is acceptable when the size of the crystal is similar to the size of the loop, but it becomes insufficient whenever the crystal is much smaller or extends beyond the loop border. Algorithms based on image analysis (*e.g.* edge detection or contrast) have thus been proposed to detect the crystal, but are not always successful and often require long processing times (Andrey *et al.*, 2004; Bern *et al.*, 2004; Roth *et al.*, 2002). Taking advantage of crystal birefringence using cross-polarized light is also possible in some cases (Echalier *et al.*, 2004). Other techniques based on scanning the entire loop for maximum diffraction intensity or X-ray fluorescence have been proposed (Jacquamet *et al.*, 2004; Karain *et al.*, 2002), but are time-consuming and may potentially damage the sample. The use of illumination wavelengths flanking the visible range has recently been considered. An elegant technique based on infrared imaging has been described which offers the advantage of being harmless to protein crystals (Snell *et al.*, 2005). Alternatively, the use of endogenous protein fluorescence has been demonstrated (Pohl *et al.*, 2004; Rosenbaum, 2000). Protein crystals illuminated with UV light emit blue light owing to the fluorescence emission of the aromatic amino acids (tryptophans, tyrosines and to a lesser extent phenylalanines). A considerable contrast enhancement results, also enabling the differentiation of protein crystals from salt crystals (Judge *et al.*, 2005). However, two difficulties have hampered the routine use of this technique. Firstly, traditional loop holders are made of nylon or other highly fluorescent polymers. The loop fluorescence may therefore confuse the crystal-detection algorithms. The second problem is that the light sources and optical setups used so far make it difficult to

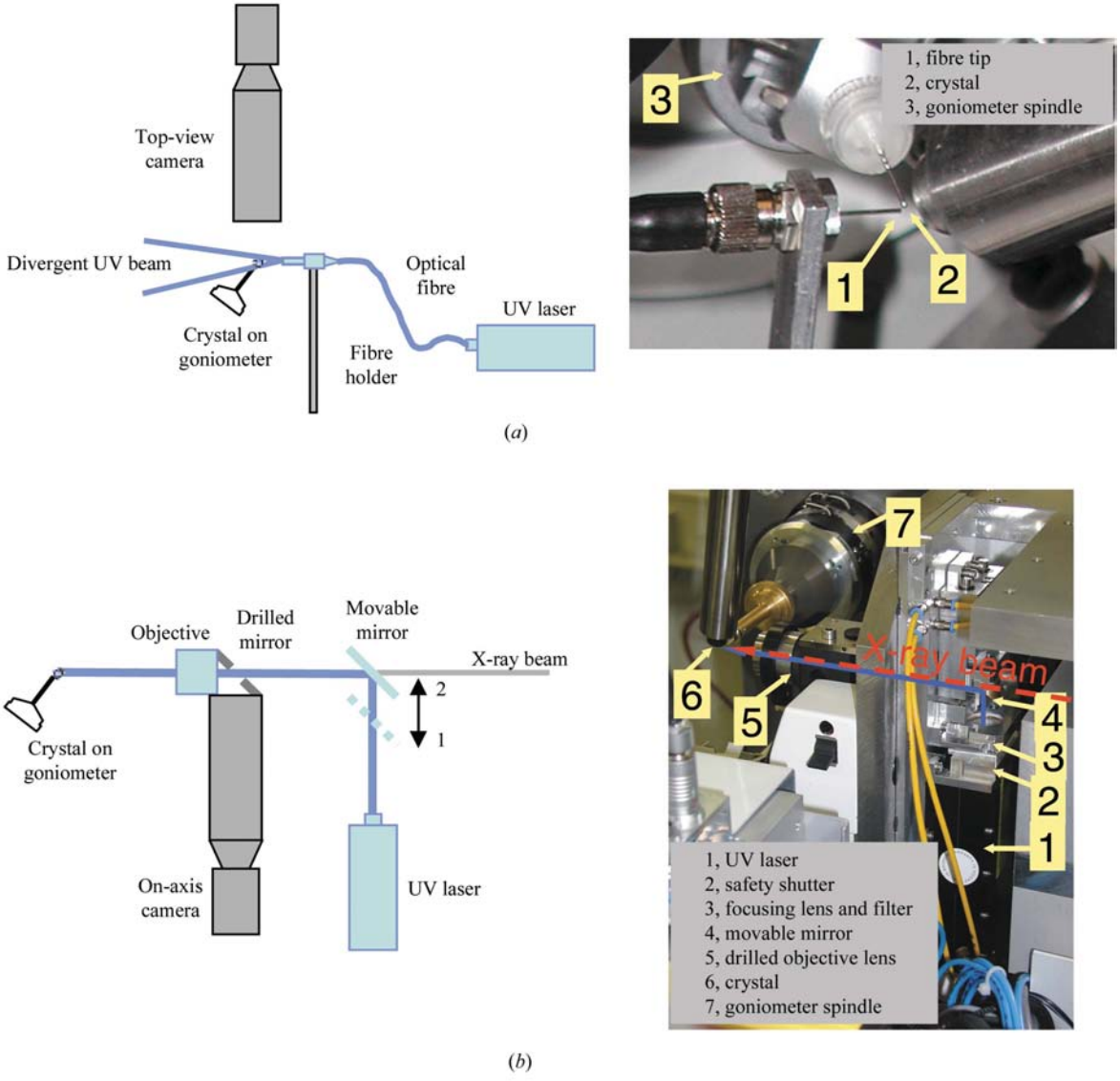

Figure 1
Sketches and photographs of the two proposed setups. (*a*) Standard setup; (*b*) on-axis setup.

gather sufficient UV power density around the sample position for quick detection of weak fluorescence. Detection of tiny crystals or weakly fluorescent crystals that, for example, do not contain tryptophan residues may therefore prove unsuccessful or at least incompatible with the speed requirements of high-throughput crystallography.

Here we propose to combine the use of short (∼20 ms) UV-laser pulses with non-fluorescent sample holders and standard visualization cameras for the detection of protein crystals mounted on synchrotron beamlines. An innovative setup is described in which the crystal is illuminated with UV light coaxial to the camera. We provide evidence that crystals are easily identified and we suggest that the proposed technique does not generate detectable UV-induced structural damage.

2. Experimental setups

We have devised crystal-illumination setups that can be combined with common goniometer geometries or with the MD2x diffractometers installed at the European Synchrotron Radiation Facility (ESRF), developed at the EMBL and commercialized by the companies Accel Instruments GmbH (Bergisch Gladbach, Germany) and Maatel (Voreppe, France). Sketches of the setups are shown in Fig. 1. The first setup (Fig. 1*a*) was used to qualify the method. The second setup (Fig. 1*b*) was developed to improve the performance of the crystal detection and to facilitate integration onto the ESRF beamlines.

2.1. Excitation laser

To excite fluorescence, ∼20 ms macropulses from a 266 nm YAG laser (JDS Uniphase Corporation) were used. This passively Q-switched laser provides ∼0.5 ns light pulses at a frequency of 8 kHz, generating an average power of ∼2 mW. The laser beam displays a Gaussian profile (0.5 mm diameter at FWHM) with a divergence of <3 mrad. This laser was chosen based on its compactness and its affordable price. Simulations of fluorescence emission by tryptophan and tyrosine residues throughout a representative protein crystal at three different excitation wavelengths (266, 280 and 300 nm) are displayed in Fig. 2 and show that 266 nm is an appropriate wavelength (see §5). An interference filter should preferably be inserted at the laser output to filter out residual visible light originating from the laser pumping diode and from harmonics of the 266 nm line. However, the data presented were obtained without such a filter.

2.2. Standard setup

An initial setup was developed at the Cryobench laboratory of the ESRF (Bourgeois *et al.*, 2002). The laser beam was coupled to a 200 µm diameter optical fibre (numerical aperture 0.22) through a collimating lens and a focusing planar convex lens. The laser, originally of class IV, was inserted

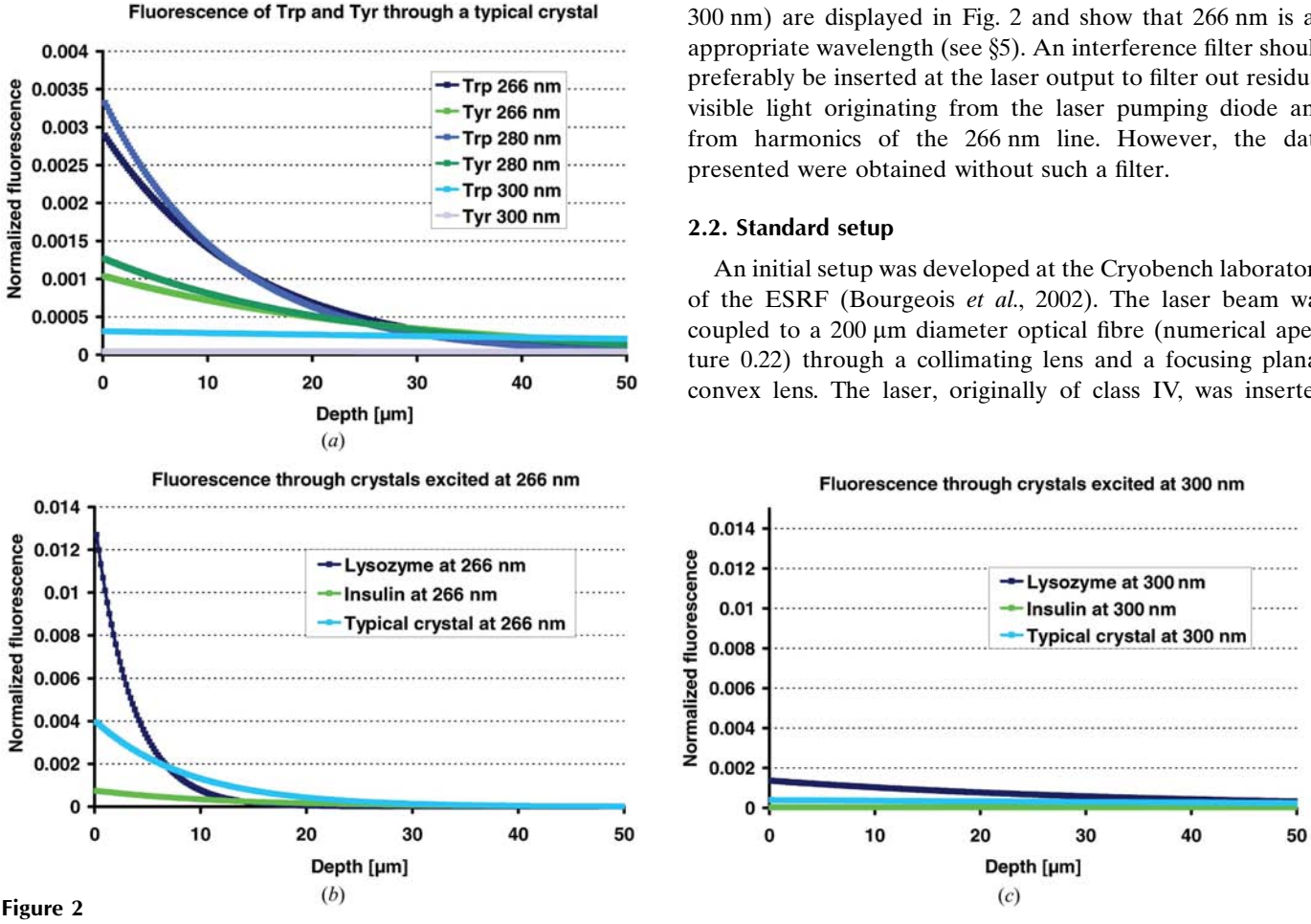

Figure 2
Simulations of fluorescence emission from protein crystals. (*a*) Contributions from tryptophan and tyrosine residues to the fluorescence emitted by a representative crystal at different excitation wavelengths (phenylalanine residues do not contribute to any appreciable extent). The representative crystal is assumed to be composed of a 10 m*M* concentration of a 500-residue protein containing 1.32% tryptophan and 3.25% tyrosine. Fluorescence profiles are reported through a 50 µm long crystal at 266, 280 and 300 nm. The illumination source is assumed to be placed on the left side of the crystals. The fluorescence intensity is normalized to the excitation intensity. (*b*) Overall fluorescence profiles from a representative crystal, tetragonal lysozyme and cubic insulin for an excitation wavelength of 266 nm. (*c*) The same profiles for a putative excitation wavelength of 300 nm. Fluorescence yields and extinction coefficients were obtained from http://omlc.ogi.edu/spectra/PhotochemCAD/html/index.html.

together with the coupling system into a closed PVC box, which at the ESRF allowed us to downclass the device to class IIIb, thus avoiding the complex safety requirements associated with class IV lasers. The other end of the fibre was inserted into a hollow needle (0.6 mm diameter, 10 mm length) and brought into the close vicinity of the sample (~0.5 mm) *via* a fibre holder comprising three micropositioning translation stages allowing precise positioning of the fibre tip. This adjustment is typically performed by looking at the fluorescence from a pre-centred nylon loop. Under such conditions, the illuminated section entirely covers a 0.3 mm diameter loop (about the largest loop used nowadays). Considering the short fibre-to-sample distance, a retractable fibre holder, for example based on a pneumatic device, is important to avoid potential collisions. This first setup has the advantage of being simple and adaptable to practically any diffractometer geometry. However, it suffers from several drawbacks: the rotation radius of the sample is limited to less than ~0.5 mm (to avoid collisions), the retractation distance must be very large if the κ geometry is used and the non-optimal laser to optical fibre coupling attenuates the transmitted UV flux. Moreover, the fibre holder cannot be easily positioned parallel to the camera viewing axis. Therefore, crystals are illuminated at an angle, which can prove non-ideal for large crystals owing to a gradient effect. Indeed, typical protein crystals strongly absorb UV light. For example, assuming a protein concentration of 10 m*M* in the crystal and ~6.6 tryptophan residues per protein molecule (the natural abundance of tryptophan is 1.32% and a protein of 500 amino acids is considered), 99% of the photons at 266 nm are absorbed within a layer of 50 µm thickness. As a consequence, a gradient in the emitted fluorescence will be observed throughout the crystal depth (Fig. 2), leading to an offset in the detected crystal centre towards the side where the UV source is located. In practice, we have noted that this problem is only severe for crystals of more than ~100 µm thickness.

2.3. On-axis setup

All the drawbacks associated with the standard setup can be overcome by illuminating the sample with a UV beam coaxial with the camera viewing axis, making no use of optical fibres. Therefore, we developed a second setup that takes advantage of the on-beam-axis video microscope that equips the ESRF MD2x diffractometers. This video microscope allows precise alignment of microcrystals with the X-ray beam by viewing the latter (using a scintillator) and the crystal without any parallax error. It is composed of a drilled objective lens whose optical axis is coaxial to the X-ray beam. The objective lens is coupled to a motorized zoom and a CCD camera by a drilled mirror set at 45°. To illuminate the sample area with the UV-laser beam, an additional device has been developed. It is composed of a movable mirror, also set at 45°, which is inserted upstream of the drilled mirror (Fig. 1*b*). When up (position 2), the mirror reflects the UV beam onto the crystal through the objective lens. When down (position 1), normal operation of the X-ray beam is restored.

In addition to improving the crystal detection, this second setup avoids the necessity of a retractable arm in the sample vicinity, eliminates the risk of collision between the crystal and the optical fibre when the crystal is not properly pre-centred and maximizes the UV flux on the crystal. However, a drawback is the additional cost related to the safety equipment necessary for using a raw UV-laser beam of class IV. The accessibility to the experimental hutch might also be restricted, depending on site regulations. However, this should not be a problem in modern fully automated beamlines where crystal handling is controlled remotely.

2.4. CCD camera

The transparency and sensitivity of standard optics and CCD cameras decrease significantly below 400 nm. However, we have found that the strong UV power density provided by the 266 nm laser makes the use of expensive optical elements and a CCD camera optimized for near-UV fluorescence imaging unnecessary. Thus, it is possible to use a single camera for both visible and UV fluorescence imaging. However, to limit UV-induced radiation damage (see below), it is important to minimize the UV dose absorbed by the sample. With this aim, the image acquisitions of the CCD camera were synchronized to the laser pulses. This allowed reduction of the pulse duration to typically ~20 ms for the on-axis setup.

With the camera used, two methods are available to further improve the detection of fluorescence. The first is to increase the gain of the CCD camera, the maximum acceptable value being limited by the noise, which affects the crystal-detection algorithms. The second method consists of using a frame-integration mode, in which multiple exposures are summed within the CCD chip before readout. This latter method is more efficient, but increases the total UV exposure of the crystals. With the on-axis setup, we found that it is sufficient to use the default one-frame mode, with medium camera gain.

2.5. Sample holders

Several sample holders were tested (Fig. 3). Standard nylon loops (Hampton Research, Aliso Viejo, CA, USA) proved to be highly fluorescent and therefore incompatible with the requirement of detection of small and weakly fluorescent protein crystals. Litholoops (Molecular Dimensions Ltd, Cambridgeshire, England) made out of Mylar are essentially non-fluorescent in the spectral range 280–450 nm, although they display a broad and weak (about 20 times less than nylon) emission line centred at 560 nm. Loops made out of Kapton (Nextal Biotechnologies, Montreal, Canada) were also tested and displayed no detectable fluorescence in the 280–450 nm range (data not shown).

2.6. Detection strategy

Considering the relatively small area illuminated by UV light, the crystal to be centred may initially be located out of the UV beam. Therefore, a pre-centring of the loop is first performed under visible light.

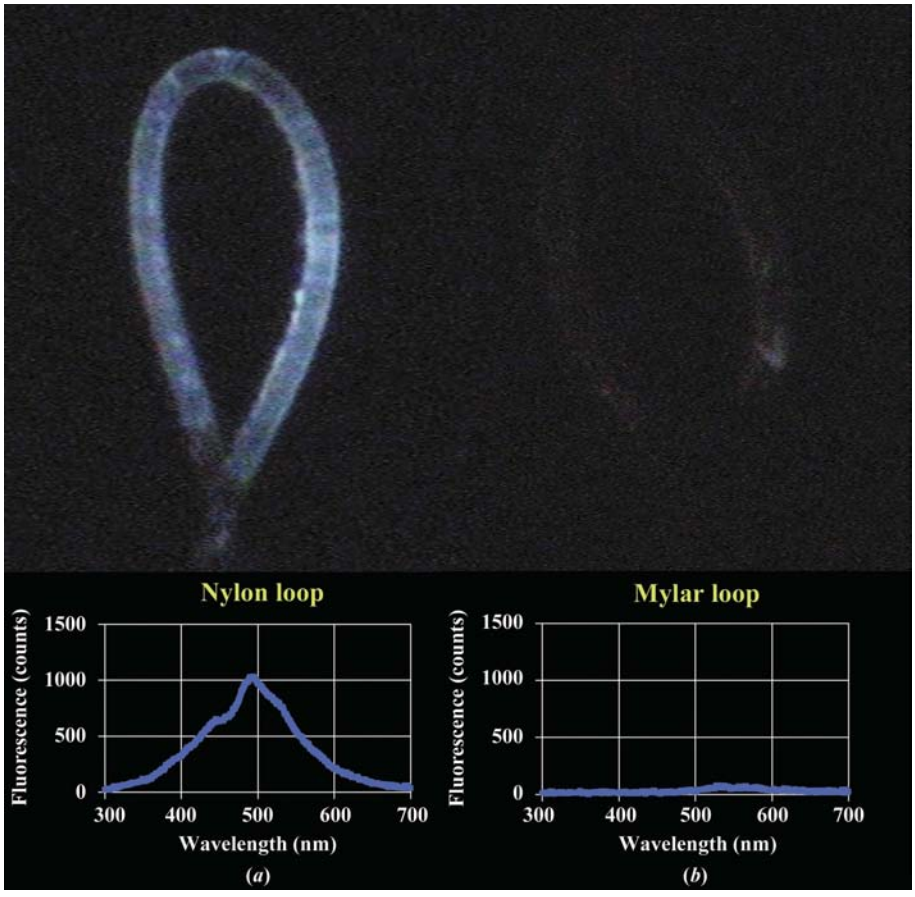

Figure 3
Fluorescence images and emission spectra from empty loops: (*a*) from a nylon loop; (*b*) from a Mylar loop. Spectra were recorded with a microspectrophotometer at the ESRF Cryobench laboratory (see http://www.esrf.fr/UsersAndScience/Experiments/MX/Cryobench/).

Once the loop is centred, fluorescence images are analysed by *C3D*, a crystal image-processing program for auto-centring, which can calculate the three-dimensional position of the crystal from a series of two-dimensional images taken during crystal rotation. The software uses two algorithms adapted to the processing of fluorescence images. The first one is based on the correlation between images and has already been described in detail (Andrey *et al.*, 2004). The second one, which was used in Figs. 4, 5 and 6, is based on a centre-of-mass calculation of the binarized images. The binarization, which converts the images into two colours, black and white, is performed at two different thresholds. The lowest threshold eliminates only the background and the highest selects only the strongest crystal signature. A quality estimator allows selection of the best threshold. The two algorithms have been found to work efficiently, even in the presence of surrounding residual fluorescence.

3. Crystallographic materials and methods

Lysozyme and insulin crystals were grown following established protocols. Using the standard setup, crystals of each protein were flash-cooled and illuminated at 100 K with 266 nm laser light for either 1 s or 1 min (with equal flux density). Crystals were then kept frozen until X-ray data collection on beamline ID23-1 at the ESRF. Lysozyme and insulin crystals belonged to the tetragonal $P4_32_12$ and cubic $I2_13$ space groups, respectively. The data were processed and scaled using *MOSFLM* and *SCALA* from the *CCP*4 suite (Collaborative Computational Project, Number 4, 1994).

The structures obtained without illumination (referred to as lyso_0sec and insu_0sec) were solved by molecular replacement with the program *MOLREP* from the *CCP*4 suite using models of triclinic lysozyme (PDB code 3lzt) and cubic insulin (PDB code 1b2d), respectively, without water molecules, as search models. Starting phases were then input to *REFMAC* (Murshudov *et al.*, 1997) and *ARP*/*wARP* (Lamzin & Wilson, 1993) and the chains were traced semi-automatically. Maximum-likelihood refinement was completed with *REFMAC* (Murshudov *et al.*, 1997) and model building with *QUANTA* (Accelrys, San Diego, C, USA). Water molecules were placed automatically with *REFMAC*/*wARP* and verified manually. The obtained models of lysozyme and insulin, without water molecules, were then used as starting models to semi-automatically trace models of lysozyme or insulin illuminated with UV light for 1 s or 1 min (referred to as lyso_1sec, lyso_60sec, insu_1sec and insu_60sec) with minimum bias. The same procedure of checking using *QUANTA* and water building using *REFMAC*/*wARP* was carried out for each model. Statistics are shown in Table 1. A last round of modelling was performed for insu_60sec, where two alternate conformations were introduced for cysteines Cys*A*7 and Cys*B*7 and their respective occupations refined.

4. Results

Fig. 4 shows representative UV-fluorescence images recorded using the standard setup. The advantage in combining the use of a UV-light source with non-fluorescent loop holders is clear. When visible light is used, a crystal of cephamycinase 2 (a class C β-lactamase, hereafter referred to as CMY2) is hardly detectable, even by the expert eye. Sophisticated image-processing software is therefore likely to fail in identifying the crystal correctly, as was the case using *C3D*. In contrast, under UV-laser illumination, the crystal is easily identified by both the user and the *C3D* software whatever the loop orientation. The advantage in using a laser source instead of a classical UV lamp (xenon–mercury or deuterium lamp) is that the image

Table 1
Effect of UV illumination at 100 K on lysozyme and insulin crystals: diffraction and refinement statistics.

Values in parentheses refer to the highest resolution shell.

	Lysozyme			Insulin		
	0 s (lyso_0sec)	1 s (lyso_1sec)	60 s (lyso_60sec)	0 s (insu_0sec)	1 s (insu_1sec)†	60 s (insu_60sec)‡
Diffraction						
Space group	$P4_32_12$			$I2_13$		
Unit-cell parameters (Å)	$a = b = 78.9$, $c = 37.0$	$a = b = 78.7$, $c = 36.9$	$a = b = 78.9$, $c = 36.9$	$a = b = c = 78.4$	$a = b = c = 78.6$	$a = b = c = 78.2$
Resolution (Å)	20–1.5 (1.58–1.5)	20–1.5 (1.58–1.5)	20–1.5 (1.58–1.5)	20–1.5 (1.58–1.5)	20–1.95 (2.0–1.95)	20–1.5 (1.58–1.5)
$R_{\rm merge}$ (%)	10.4 (28.3)	6.5 (18.7)	5.6 (19.4)	6.8 (39.6)	6.0 (42.1)	7.4 (38.1)
Completeness	99.9 (100)	99.9 (100)	99.8 (100)	100 (100)	94.6 (100)	100 (100)
$I/\sigma(I)$	17.5 (6.5)	27.0 (12.2)	29.0 (13.6)	29.4 (9.3)	32.4 (6.8)	30.0 (10.0)
Multiplicity	10.4 (10.6)	10.4 (10.4)	10.4 (10.5)	16.2 (16.3)	10.3 (10.6)	16.1 (16.2)
Refinement						
No. of residues	128	129	129	*A*, 21; *B*, 28	*A*, 21; *B*, 29	*A*, 21; *B*, 28
No. of waters	45	133	134	79	31	52
R factor/$R_{\rm free}$§ (%)	23.2/24.7	19.6/20.8	18.9/20.0	20.5/22.5	20.7/23.0	20.7/21.9
R.m.s.d. on bond length (Å)	0.009	0.009	0.008	0.009	0.008	0.010
R.m.s.d. on bond angles (°)	1.187	1.176	1.161	1.047	0.929	1.070
R.m.s.d. on C^α only (Å)	0 (reference)	0.065	0.085	0 (reference)	0.081	0.030
Lysozyme B factor (Å^2)						
Average	13.66	14.67	13.43			
Cys6 S^γ–Cys127 S^γ	17.42–17.59	17.35–17.61	16.00–16.16			
Cys30 S^γ–Cys115 S^γ	9.66–10.46	9.25–9.95	9.15–9.54			
Cys64 S^γ–Cys80 S^γ	9.34–8.43	9.04–8.17	10.10–9.14			
Cys76 S^γ–Cys94 S^γ	12.53–11.30	12.35–11.21	11.45–10.91			
Insulin B factor (Å^2)						
Average				15.83	28.46¶	15.84
Cys*A*6 S^γ–Cys*A*11 S^γ				11.13–11.55	27.43–27.25	12.76–13.05
Cys*A*7 S^γ–Cys*B*7 S^γ				14.24–14.19	27.06–28.50	17.84 −17.18
Cys*A*20 S^γ–Cys*B*19 S^γ				10.64–9.04	27.53–26.40	14.4–10.42

† This crystal diffracted to lower resolution than insu_0sec and insu_60sec for reasons that are likely to be related to a lower intrinsic crystal quality. ‡ Values given before a final round of occupancy refinement with alternate conformations for cysteines Cys*A*7 and Cys*B*7. § Calculated with 5% randomly selected reflections excluded from refinement. ¶ These values should not be compared with those from insu_0sec and insu_60sec owing to the lower resolution of the data.

can be collected more quickly owing to the increased power density available at the sample location. The protein CMY2 contains 3.6% tryptophan residues, a quite favourable case in yielding significant fluorescence. Although it is likely that satisfactory images could have been recorded with a UV lamp on CMY2, this is more questionable in the case of insulin. Insulin is a protein that lacks tryptophan and in this case UV fluorescence only arises from tyrosine residues, which display a significantly lower extinction coefficient and fluorescence quantum yield. Remarkably, insulin crystals can still be detected by taking advantage of the photon flux delivered by a laser, whereas with our standard camera optics they remain invisible when the laser is replaced by a deuterium UV lamp (Mikropack DH-2000-BAL, UV power density at sample position about 1000 times inferior to our UV laser; Fig. 5). In this context, it is important to note that 15% of the structures deposited in the Protein Data Bank do not contain tryptophans.

The advantages of using the on-axis setup are shown in Fig. 6. Fig. 6(*a*) shows a large lysozyme crystal illuminated sideways by a standard setup and Fig. 6(*b*) a comparable crystal illuminated on-axis. Clearly, the crystal centre as detected by *C3D* is more accurate in the second case, since the gradient effect evident in Fig. 6(*a*) does not perturb the analysis of the image in Fig. 6(*b*) (although it is of course still present along the depth of that image). A fluorescence image from an insulin crystal is also displayed in Fig. 6(*c*), emphasizing the high sensitivity resulting from the brighter UV light provided by direct optical coupling. This high-contrast image was acquired with a single UV flash of 20 ms and the default camera gain and can be compared with Fig. 5(*b*), which required a higher camera gain. In total, we expect to be able to detect a very wide range of crystals using the on-axis setup, from large to tiny crystals exhibiting strong or weak fluorescence.

The use of UV-laser light to visualize protein crystals poses the question of potential UV-induced radiation damage and associated structural modifications. Indeed, previous work has shown that proteins in general are sensitive to UV light (Wien *et al.*, 2005). In our case, the standard setup generates a significant power density at the sample position (about 5 mW mm^{-2} or 6.75 $\times$ 10^{15} photons s^{-1} mm^{-2}; this power density is approximately doubled with the on-axis setup). Therefore, we have addressed this potential problem by recording diffraction data from lysozyme and insulin crystals illuminated with the standard setup for 1 s (corresponding to a total exposure of 6.75 $\times$ 10^{15} photons mm^{-2}) and 60 s (total exposure of 4.05 $\times$ 10^{17} photons mm^{-2}) at 100 K and comparing the obtained structures with those from non-illuminated crystals. The results are presented in Fig. 7 and Table 1. They clearly show that extended illumination, although without a noticeable effect on diffraction statistics, damages proteins in a manner comparable to X-rays. For

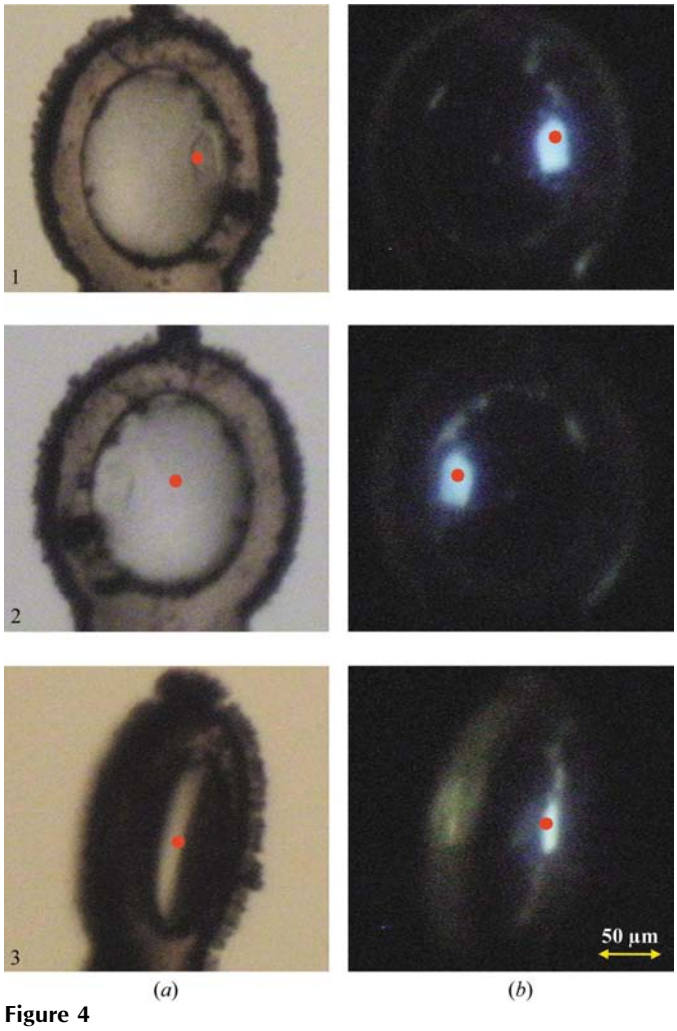

Figure 4
Fluorescence images recorded with the standard setup. A crystal of cephamycinase 2 (~20 µm in thickness) is shown in three different orientations in visible light (*a*) or UV light (*b*). Red points show the crystal centre as detected by the *C3D* software. The crystal is hardly detectable in visible light, so that *C3D* fails to identify it correctly in orientations 2 and 3. In contrast, the crystal is easily identified under UV-laser illumination by both the user and the software, whatever the loop orientation.

example, in the case of insulin, despite the relative transparency of these crystals to UV photons owing to the absence of tryptophan residues, all disulfide bridges are damaged upon a 60 s exposure to 266 nm radiation (Fig. 7). The reduction of disulfide bridges is accompanied by clear motion of some of the adjacent main-chain carbonyl O atoms. However, structural refinement suggests that the damage is limited to only a fraction of the molecules within the crystal. This is indicated by the successful modelling of unperturbed disulfide bridges in the insu_60sec structure, as judged by final density maps (not shown), by overall $R_{\rm cryst}$ and $R_{\rm free}$ factors and by the only moderate increase in the *B*-factor values of cysteines when compared with the insu_0sec structure (Table 1). A final round of occupancy refinement suggests that ~20% of the Cys*A*7–Cys*B*7 disulfide bridges in the crystal have been ruptured. In the case of lysozyme, the damage appears much less pronounced upon a 60 s illumination (Table 1), but this could

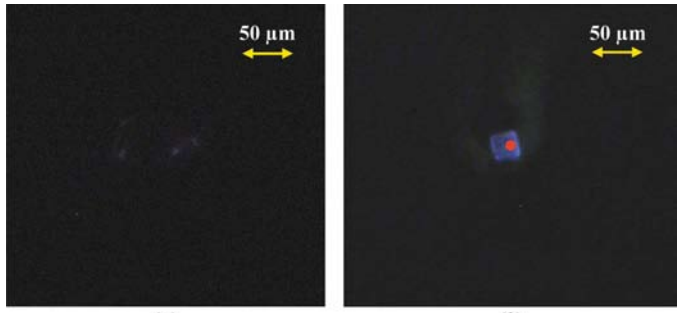

Figure 5
Improvement using a UV laser. A crystal of insulin is shown under UV light generated by a deuterium lamp (*a*) or by a UV laser at 266 nm (*b*). The crystal is not detectable with the deuterium lamp owing to the lack of power density. In contrast, the crystal is easily identified under UV-laser illumination by the user or by the *C3D* software (red point).

partly arise from the gradient effect that prevents the penetration of UV photons into the bulk of the crystal.

Fortunately, both types of crystals show very limited damage upon a 1 s illumination: the details of the structures are not modified to any appreciable level at the resolution of our data (see the featureless difference electron-density map of Fig. 7*a* and Table 1). Nevertheless, we suggest that crystals to be detected by the proposed protocols should not be illuminated with our 266 nm laser for more than 1 s (corresponding to a total exposure of 6.75×10^{15} photons mm^{-2}) and preferably for less. This should not pose any problem, as the exposure time used to collect the images shown in Figs. 4, 5 and 6 was equal to 20 ms (total exposure of 1.35×10^{14} photons mm^{-2}).

5. Discussion

We have shown that the combined use of a standard camera and optics, non-fluorescent sample holders and a UV laser to excite the fluorescence of aromatic residues is an efficient tool for the visualization of protein crystals mounted on synchrotron beamlines. It facilitates the unambiguous identification of the crystal in cases where too poor a contrast is obtained with visible light. Short laser pulses (~20 ms) are sufficient to detect small samples of up to a few micrometres in size even when they are devoid of tryptophan residues. The on-axis setup installed on the ESRF macromolecular crystallography beamlines provides an optimum contrast for fluorescence images and overcomes the gradient effect on large crystals while minimizing parallax errors.

An immediate application of the technique is to give crystallographers an option to collect UV-fluorescence images of their sample in cases where they fail to identify the crystal with visible light. These images may then be used in a manual centring procedure such as the 'three-click procedure' available on the MD2x diffractometers of the ESRF beamlines.

In the context of automation, the proposed method is expected to improve the score of existing procedures, as demonstrated in Fig. 4 for the case of the *C3D* software. For the reliable detection of the most difficult samples, a series of

laser shots could be collected at several crystal orientations (typically ∼5) in order to provide a comprehensive set of images for global analysis. It could also be envisaged to reconstruct the three-dimensional shape of the crystals from such images, *e.g.* to correct for the effect of crystal absorption when long X-ray wavelengths are used.

Another application, previously proposed in the case of the analysis of crystallization trays (Judge *et al.*, 2005) is the possibility of discriminating against salt crystals, which do not fluoresce. Crystals containing cofactors such as NADPH would also be immediately detectable as they may strongly fluoresce depending on their redox state.

In using the technique successfully, a number of precautions must be taken. Owing to the limited size of the UV-illuminated area, a preliminary centring of the loop under visible light is useful. Importantly, non-fluorescent loops need to be clean enough so that the analysis program is not confused by possibly highly fluorescent impurities sticking to them. Although this is a rare case, if large amounts of non-crystalline protein are present in the crystallization solution (for example as an aggregated 'skin'), care should be taken to eliminate them during soaking with cryoprotectants. Finally, proteins and nucleic acids are sensitive to UV radiation and can only withstand a limited exposure before structural damage occurs.

The 266 nm wavelength chosen in this work achieves a satisfactory compromise between fluorescence strength (Fig. 2) and laser compactness and cost. However, the strong absorption of UV light at such a wavelength by biological material generates a fluorescence gradient along the direction of illumination, creating a potential difficulty in the analysis of images from large optically thick crystals. A major advantage of the on-axis setup is that its design allows one to overcome this problem. To avoid the gradient effect with the standard setup, a longer wavelength, *e.g.* ∼300 nm, could be proposed (Fig. 2). Such a wavelength, however, would produce much

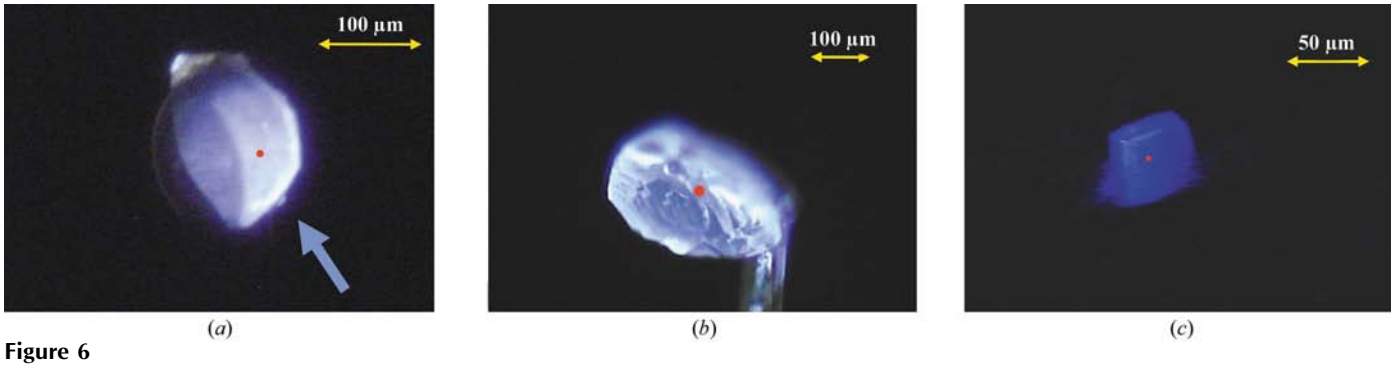

Figure 6
Improvement using the on-axis setup. Fluorescence images of lysozyme crystals recorded with the standard setup (*a*) or with the on-axis setup (*b*) are shown. In (*a*), the blue arrow shows the direction of illumination. A clear gradient in the emitted light is seen along this direction. In (*b*), the gradient effect is along the depth of field and is therefore not visible. As a consequence, the crystal centre detected by the *C3D* software (red point) is more accurate. (*c*) Fluorescence image from an insulin crystal recorded with the on-axis setup. This image was recorded in 20 ms and shows excellent contrast considering that insulin is devoid of tryptophan residues.

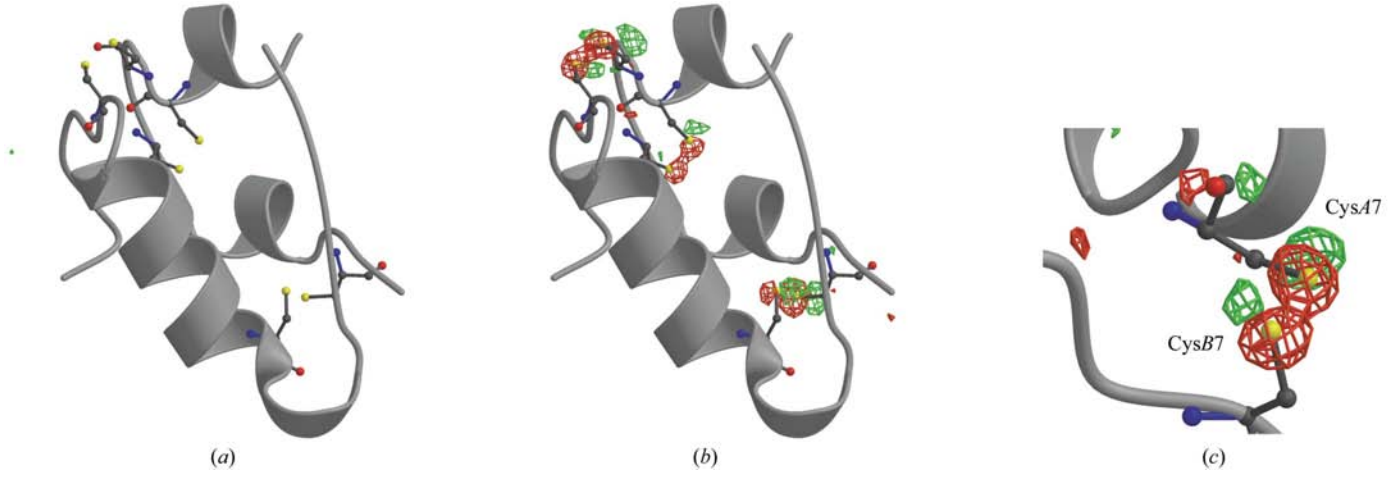

Figure 7
Effect of UV-induced radiation damage. Experimental difference electron-density maps ($F_{\rm obs\text{-}UV} - F_{\rm obs\text{-}noUV}$) are shown for insulin. Maps are contoured at $\pm 5.0\sigma$, where σ is the standard deviation of the electron-density difference (red, negative; green, positive) and are overlaid on a model of non-irradiated insulin. (*a*) Overall view of the protein for a 1 s exposure to 266 nm laser light (the same difference map displayed at $\pm 3.0\sigma$ is also featureless and shows only noise peaks). (*b*) The same view of the protein for a 60 s exposure to 266 nm laser light (with identical power density as in *a*). (*c*) Example of a damaged disulfide bridge. Breakage of the Cys*A*7–Cys*B*7 bridge is clearly visible, together with a significant displacement of the main-chain carbonyl group of Cys*A*7. The maps were calculated using *CCP*4 (Collaborative Computational Project, Number 4, 1994). This figure was drawn using *BOBSCRIPT* (Esnouf, 1999) and *RASTER3D* (Merritt & Bacon, 1997).

weaker fluorescence in general and no fluorescence at all for proteins devoid of tryptophan residues.

The combined use of a powerful UV laser with standard camera optics is an efficient, simple, compact and cost-effective solution to visualize protein crystals mounted in non-fluorescent loops. Other solutions are possible, such as combining a polychromatic UV-light source (deuterium lamp or xenon–mercury arc lamp) with optics optimized for UV/blue light and cooled CCD sensors. Such solutions offer the advantage of practically eliminating the radiation-damage issue. However, the long exposure times required for samples with weak fluorescence are not compatible with the demands of high-throughput crystallography. Also, in such cases very weak fluorescence levels might be drowned in the residual visible light present in the experimental cabin. Finally, only a laser makes the implementation of the on-axis setup easy, with the advantages of not affecting the sample environment and giving gradient-free fluorescence images.

In conclusion, the combination of a UV-laser with a camera optimized for UV/blue light would offer an ideal solution, allowing the use of sub-millisecond exposure times and preventing UV radiation damage altogether. In its present state, our technique already offers a new opportunity to overcome one of the major bottlenecks in automated structural proteomics.

We thank Cedric Bauvois for providing crystals of cephamycinase 2 and José-Antonio Marquez for providing crystals of insulin and lysozyme.

References

Abola, E., Kuhn, P., Earnest, T. & Stevens, R. C. (2000). *Nature Struct. Biol.* **7**, *Suppl.*, 973–977.

Andrey, P., Lavault, B., Cipriani, F. & Maurin, Y. (2004). *J. Appl. Cryst.* **37**, 265–269.

Bern, M., Goldberg, D., Stevens, R. C. & Kuhn, P. (2004). *J. Appl. Cryst.* **37**, 279–287.

Bourgeois, D., Vernede, X., Adam, V., Fioravanti, E. & Ursby, T. (2002). *J. Appl. Cryst* **35**, 319–326.

Cohen, A. E., Ellis, P. J., Miller, M. D., Deacon, A. M. & Phizackerley, R. P. (2002). *J. Appl. Cryst.* **35**, 720–726.

Collaborative Computational Project, Number 4 (1994). *Acta Cryst.* D**50**, 760–763.

Echalier, A., Glazer, R. L., Fülöp, V. & Geday, M. A. (2004). *Acta Cryst.* D**60**, 696–702.

Esnouf, R. M. (1999). *Acta Cryst.* D**55**, 938–940.

Holton, J. & Alber, T. (2004). *Proc. Natl Acad. Sci. USA*, **101**, 1537–1542.

Jacquamet, L., Ohana, J., Joly, J., Borel, F., Pirocchi, M., Charrault, P., Bertoni, A., Israel-Gouy, P., Carpentier, P., Kozielski, F., Blot, D. & Ferrer, J.-L. (2004). *Structure*, **12**, 1219–1225.

Judge, R. A., Swift, K. & Gonzalez, C. (2005). *Acta Cryst.* D**61**, 60–66.

Karain, W. I., Bourenkov, G. P., Blume, H. & Bartunik, H. D. (2002). *Acta Cryst.* D**58**, 1519–1522.

Kim, Y., Dementieva, I., Zhou, M., Wu, R., Lezondra, L., Quartey, P., Joachimiak, G., Korolev, O., Li, H. & Joachimiak, A. (2004). *J. Struct. Funct. Genomics*, **5**, 111–118.

Lamzin, V. S. & Wilson, K. S. (1993). *Acta Cryst.* D**49**, 129–147.

Lesley, S. A. *et al.* (2002). *Proc. Natl Acad. Sci. USA*, **99**, 11664–11669.

Liu, Z. J., Lin, D., Tempel, W., Praissman, J. L., Rose, J. P. & Wang, B.-C. (2005). *Acta Cryst.* D**61**, 520–527.

McPherson, A. (2004). *J. Struct. Funct. Genomics*, **5**, 3–12.

Merritt, E. A. & Bacon, D. J. (1997). *Methods Enzymol.* **277**, 505–524.

Murshudov, G. N., Vagin, A. A. & Dodson, E. J. (1997). *Acta Cryst.* D**53**, 240–255.

Ness, S. R., de Graaff, R. A., Abrahams, J. P. & Pannu, N. S. (2004). *Structure*, **12**, 1753–1761.

Ohana, J., Jacquamet, L., Joly, J., Bertoni, A., Taunier, P., Michel, L., Charrault, P., Pirocchi, M., Carpentier, P., Borel, F., Kahn, R. & Ferrer, J.-L. (2004). *J. Appl. Cryst.* **37**, 72–77.

Panjikar, S., Parthasarathy, V., Lamzin, V. S., Weiss, M. S. & Tucker, P. A. (2005). *Acta Cryst.* D**61**, 449–457.

Pohl, E., Ristau, U., Gehrmann, T., Jahn, D., Robrahn, B., Malthan, D., Dobler, H. & Hermes, C. (2004). *J. Synchrotron Rad.* **11**, 372–377.

Rosenbaum, G. (2000). *Workshop on Techniques for Automatic Mounting, Viewing and Centering of Pre-cooled Protein Crystals*, 11–12 May 2000, SSRL, Stanford, USA.

Roth, M., Carpentier, P., Kaikati, O., Joly, J., Charrault, P., Pirocchi, M., Kahn, R., Fanchon, E., Jacquamet, L., Borel, F., Bertoni, A., Israel-Gouy, P. & Ferrer, J.-L. (2002). *Acta Cryst.* D**58**, 805–814.

Snell, E. H., van der Woerd, M. J., Miller, M. D. & Deacon, A. M. (2005). *J. Appl. Cryst.* **38**, 69–77.

Snell, G., Cork, C., Nordmeyer, R., Cornell, E., Meigs, G., Yegian, D., Jaklevic, J., Jin, J., Stevens, R. C. & Earnest, T. (2004). *Structure*, **12**, 537–545.

Stevens, R. C. (2000). *Curr. Opin. Struct. Biol.* **10**, 558–563.

Stevens, R. C., Yokoyama, S. & Wilson, I. A. (2001). *Science*, **294**, 89–92.

Terwilliger, T. C. *et al.* (2003). *Tuberculosis*, **83**, 223–249.

Wien, F., Miles, A. J., Lees, J. G., Vronning Hoffmann, S. & Wallace, B. A. (2005). *J. Synchrotron Rad.* **12**, 517–523.

Yokoyama, S. (2003). *Curr. Opin. Chem. Biol.* **7**, 39–43.